Simulating Organogenesis: Algorithms for the Image-based Determination of Displacement Fields

CLEMENS ARTHUR SCHWANINGER, ETH Zurich
DENIS MENSHYKAU, ETH Zurich
DAGMAR IBER, ETH Zurich

arXiv:1410.4452v1 [q-bio.QM] 16 Oct 2014

Recent advances in imaging technology now provide us with 3D images of developing organs. These can be used to extract 3D geometries for simulations of organ development. To solve models on growing domains, the displacement fields between consecutive image frames need to be determined. Here we develop and evaluate different landmark-free algorithms for the determination of such displacement fields from image data. In particular, we examine minimal distance, normal distance, diffusion-based and uniform mapping algorithms and test these algorithms with both synthetic and real data in 2D and 3D. We conclude that in most cases the normal distance algorithm is the method of choice and wherever it fails, diffusion-based mapping provides a good alternative.

ACM Reference Format:
C. Arthur Schwaninger, Denis Menshykau, Dagmar Iber, 2014. Simulating Organogenesis: Algorithms for the Image-based Determination of Displacement Fields *ACM Trans. Embedd. Comput. Syst.* 9, 4, Article 39 (January 2014), 21 pages.
DOI: http://dx.doi.org/10.1145/0000000.0000000

1. INTRODUCTION

During the development of multicellular organisms, patterns emerge that result in the appearance of body axes, organs, appendages and other functional structures. While many of the responsible genes have been identified, it is still unclear how the patterning processes are controlled in time and space and the regulatory processes are typically too complex to be addressed by verbal reasoning alone. Mathematical models have a long history in developmental biology [Turing 1952; Wolpert 1969], but have long been difficult to test experimentally. Recent technical advances now yield an increasing amount of quantitative data [Oates et al. 2009; Wartlick et al. 2009; Wartlick et al. 2011], and now permit the generation of more detailed, data-based and testable models [Iber and Zeller 2012; Morelli et al. 2012].

We and others have developed mathematical models for a range of developmental processes as recently reviewed in [Iber and Menshykau 2013; Iber and Germann 2014], including the control of branching morphogenesis [Menshykau et al. 2012; Celliere et al. 2012; Menshykau and Iber 2013], limb development [Probst et al. 2011; Badugu et al. 2012] and bone development [Tanaka and Iber 2013]. The models are based on

This work is supported by SystemsX grants of the Swiss National Fund (SNF).
Author's addresses: C.A. Schwaninger, D. Menshykau and D. Iber, D-BSSE, ETH Zurich, Mattenstrasse 26, 4058 Basel, Switzerland; Swiss Institute of Bioinformatics (SIB), Switzerland.
Permission to make digital or hard copies of part or all of this work for personal or classroom use is granted without fee provided that copies are not made or distributed for profit or commercial advantage and that copies show this notice on the first page or initial screen of a display along with the full citation. Copyrights for components of this work owned by others than ACM must be honored. Abstracting with credit is permitted. To copy otherwise, to republish, to post on servers, to redistribute to lists, or to use any component of this work in other works requires prior specific permission and/or a fee. Permissions may be requested from Publications Dept., ACM, Inc., 2 Penn Plaza, Suite 701, New York, NY 10121-0701 USA, fax +1 (212) 869-0481, or permissions@acm.org.
© 2014 ACM 1539-9087/2014/01-ART39 $15.00
DOI: http://dx.doi.org/10.1145/0000000.0000000

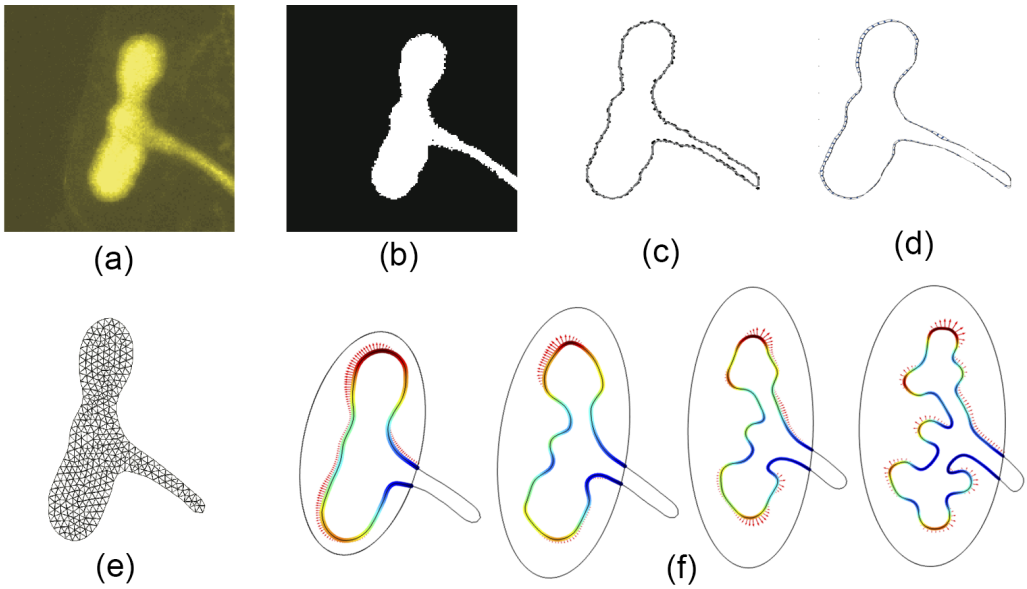

Fig. 1: **The Image-Based Modelling Approach.** a) an image of mouse embryonic kidney explant, b) segmented image, c) extracted border in the shape of the embryonic kidney explant, d) displacement field, e) computational mesh and f) solution of a computational model on a growing domain. Adapted from [Adivarahan et al. 2013].

partial differential equations (PDEs) of the form

$$\dot{c}_\mathrm{i} = D_\mathrm{i}\Delta c_\mathrm{i} + R(c_1, \ldots, c_n) \tag{1}$$

where $\dot{c}_\mathrm{i}$ denotes the time derivative of c_i, c_i denotes the concentration of the different species i, D_i represents the diffusion coefficient of species i, Δ the Laplace operator, and $R(c_1, \ldots, c_n)$ the biochemical reactions between the n different species $i \in [1, n]$. Parameter values for the models are set so that embryonic gene expression and signalling patterns from wild type and mutant mice can be reproduced on the idealised 2D and 3D domains. To further increase the accuracy and thus the predictive power of the models, it is important to solve them on realistic embryonic geometries. Recent advances in imaging technology, algorithms and computer power now permit the development of such increasingly realistic simulations of biological processes. In particular, it is now possible to obtain 2D and 3D shapes of developing organs and to solve the models on those embryonic geometries [Gleghorn et al. 2012; Clément et al. 2012; Menshykau et al. 2014; Iber et al. 2015].

During embryonic development, growth and patterning are tightly linked [Iber et al. 2015]. It is therefore insufficient to solve the reaction-diffusion equations on a static domain. When solving Eq. 1 on a growing domain, we need to include advection and dilution terms [Iber et al. 2015] and obtain

$$\dot{c}_\mathrm{i} + \nabla(\mathbf{u} \cdot c_\mathrm{i}) = D_\mathrm{i}\Delta c_\mathrm{i} + R(c_1, \ldots, c_n). \tag{2}$$

Here, $\mathbf{u}$ represents the velocity field of the moving domain. To develop a mechanistic model of growth control that yields $\mathbf{u}$, we would need to understand how growth is controlled at the molecular level during development. This is not yet the case, and recent measurements demonstrate that simple growth models [Dillon and Othmer

1999] fail to correctly predict shape changes during developmental growth [Boehm et al. 2010]. Alternatively, one could measure $\mathbf{u}$ for biological systems by tracking cell division and cell movements in the growing domain. So far, this has been done only in very few experimental systems, e.g. [Bellaïche et al. 2011]. To obtain an estimate of $\mathbf{u}$ for our experimental systems of interest, we therefore use imaging data at different stages of the deformation process to estimate the local rates of tissue deformation [Adivarahan et al. 2013]. An example of a snapshot of such a 2D time series is shown in Figure 1a. To extract the local rates of tissue deformation from the available imaging data, we segment the images (Fig. 1b) and extract the borders in 2D or surfaces in 3D from the images (Fig. 1c). We then need to determine a displacement field that maps the earlier border or surface on the later border or surface (Fig. 1d). Once we have this displacement field between the boundaries of the two subsequent geometries, we can use this in our simulations. To this end, we read the initial geometry and the displacement field into the PDE solver (in our case COMSOL [Menshykau and Iber 2012]). We then mesh the computational domain (Fig. 1e). Finally, we solve the model given by Eq. 2 on the embryonic, growing domain (Fig. 1f). While solving the model, the PDE solver deforms the boundary according to the displacement field, and passively stretches the domain to follow the deforming boundary. The deformation inside the domain yields the velocity field $\mathbf{u}$. It is important to note that in this way, we obtain a deformation that recapitulates the embryonic shape changes. However, since experimental data is missing that would yield information on the movement of boundary and internal points, both the mapping of the boundary points and the deformations inside the domain, and thus the velocity field $\mathbf{u}$, are arbitrary and therefore do not necessarily correspond to the physiological changes. For sufficiently small deformations, i.e. for sufficiently small time steps between boundaries, the error can, however, be expected to be sufficiently small such that we still obtain useful results.

Since the choice of displacement field is arbitrary, it is desirable that the mapping algorithm delivers a displacement field that facilitates simulations and that works automatically without any further user input. Many algorithms have been proposed to address this issue, e.g. [Lazarus and Verroust 1998; Alexa 2002; Sigal et al. 2008; Athanasiadis et al. 2010]. However, algorithms that work also for non-convex surfaces (such as branching geometries) without user input are rare, and will be computationally costly if generally applicable [Lazarus and Verroust 1998]. The commercial software package AMIRA, which we used previously [Menshykau et al. 2014], offers the landmark based Bookstein algorithm [Bookstein 1989]. However, the Bookstein algorithm requires the manual identification of points of correspondence, so-called landmarks, which leads to *ad hoc* rather than algorithmic displacement fields and requires a lot of manual work. We have previously also used a minimal distance based algorithm, which is straight-forward to implement, but which frequently fails to deliver useful displacement fields and then requires manual curation [Adivarahan et al. 2013]. To overcome these drawbacks, we developed four basic algorithms and their extensions that can be used to calculate the displacement field between two consecutive stages without any user input. We introduce a quality measure to evaluate our algorithms and test the algorithms with image data for kidney and lung branching morphogenesis.

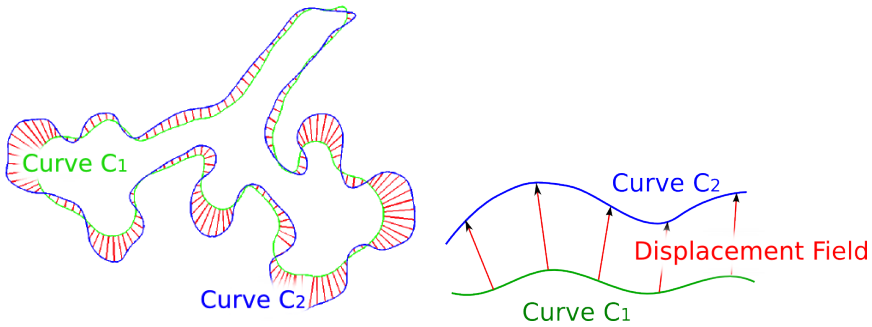

(a) Displacement field of entire domain (b) Local displacement field

Fig. 2: **Displacement Field.** Curve C_1 represents the shape of an embryonic structure at a time step t; curve C_2 represents the same structure at a later time point $t+\Delta t$. For our simulations of growing organs it is essential to find a high quality displacement field that maps points from C_1 to C_2. (a) An example of the displacement field for the entire growing embryonic kidney explant. (b) The displacement field at some local position of the domain shown in panel (a).

2. ALGORITHMS FOR COMPUTING THE DISPLACEMENT FIELDS

2.1. Basic Algorithms

We denote the curve at time t by C_1 and the curve at time $t + \Delta t$ by C_2 as shown in Figure 2. Prior to the calculation of the displacement field we interpolated the set of discrete points on C_1 and C_2 such that both curves contain the same number of points that were equally spaced on each curve. Here we used the MATLAB function `interparc` [D'Errico 2012b] and we used spline interpolation for smooth curves and linear interpolation in case of corner points. The interpolated points were then mapped using one of the following basic algorithms. In Section 2.2 we will show how these algorithms can be extended.

(1) *Minimal Distance Mapping:* Every point on the curve C_1 is mapped to the point on the curve C_2 to which it has the minimal distance. The point on C_2 can be determined using the MATLAB function `distance2curve` [D'Errico 2012a].
(2) *Normal Mapping:* The normal vector is determined at every point on C_1 and is mapped to the closest point on C_2 where the normal and C_2 intersect.
(3) *Diffusion Mapping:* This mapping is obtained by solving the steady state diffusion equation (Laplace equation)

$$\Delta c = 0, \tag{3}$$

which follows from Eq. 1 in steady state ($\dot{c} = 0$) and in the absence of reactions ($R = 0$). Eq. 3 is solved in the area between the two curves in 2D, or between two surfaces in 3D using COMSOL Multiphysics (Fig. 3a). As initial conditions we use Dirichlet boundary conditions and we set the value c to be 1 on C_1 and 0 on C_2 or *vice versa*. The start and end points on C_1 and C_2 are determined by computing the streamlines using particle tracking (Fig. 3b); the start and end points define the mapping vector (Fig. 3c).
(4) *Uniform Mapping:* For this algorithm we need at least one point on C_1 and one point on C_2, for which we know that they should be mapped onto each other. These two points can either be selected manually or algorithmically. To determine such points algorithmically, one could use curve intersection points in case of intersecting curves, or in case of open, non-intersecting curves, beginning and end points.

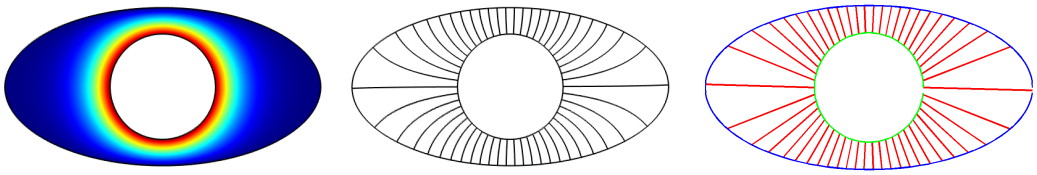

(a) Solution of the diffusion equation (b) Streamlines (c) Diffusion mapping

Fig. 3: **Diffusion Mapping**. (a) The numerical solution of the diffusion equation. (b) The streamlines, as obtained by particle tracking from C_1 to C_2. (c) The displacement field vectors are obtained by connecting start and end points of the streamlines.

If the mapping has been defined for at least one single point, we can interpolate N points equidistantly along both curves, starting from the predefined point and ending at the same point (for closed curves) or at another predefined point (for open curves or curve segments). We used the MATLAB function `interparc` to calculate the N equidistant points on a curve.

2.2. Extensions

In some cases, prior to computing the displacement field with one of the basic algorithms, the following additional steps can improve the quality of the resulting displacement field.

(1) *Reverse Mapping:* The mapping can be done from curve C_2 to C_1.
(2) *Transformation of C_1:* The more similar the two curves C_1 and C_2 are, the easier it is to find a good displacement field and the less it depends on which of the four above mentioned algorithms we choose. Examples include cases where not only the shape, but also the lengths of the curves differ. It can then be beneficial to first perform linear operations that transform the curve C_1 to curve $C_{1,\mathrm{t}}$, from which we then compute the displacement field $\mathcal{D}_\mathrm{t}$. Finally, we invert the transformation and compute the displacement field $\mathcal{D}$ for the original curves C_1 to C_2. A detailed description of our algorithm can be found in Appendix A.
(3) *Curve Segment Mapping* Curves C_1 and C_2 can have intersection points (Fig. 2a) and it is then often beneficial to first split the domain based on the intersection points into a set of subdomains, where the basic mapping routines are carried out independently. Figure 4 shows the displacement fields that were computed with the normal mapping algorithm when intersection points were either ignored (Fig. 4a) or used to split the domain into independent subdomains (Fig. 4b). If the intersection points are ignored, then many points are mapped in the wrong direction because the algorithm maps to the closest normal intersection point. This issue can be resolved if curves are split into segments according to the intersection points (Fig. 4b).

3. EVALUATION

3.1. Qualitative Evaluation of the Mapping Algorithms

Here we present results of a qualitative evaluation of the basic mapping algorithms. We first consider the simple case of mapping a circle onto a larger ellipse (Fig. 5).

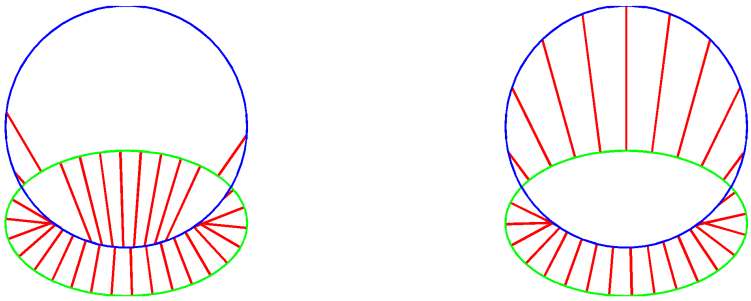

(a) Global mapping (b) Segment mapping

Fig. 4: **Mapping of Curves with Intersections**. (a) The displacement field was computed globally using normal mapping. Note that many points map to the wrong segment on C_2. (b) The curves were split into subdomains based on the intersection points and only segments were mapped onto each other using normal mapping. The mappings are now correct.

— *Minimal Distance:* Mappings based on the minimal distance between two points are easy to implement but prone to errors since the algorithm only gives good results if the domain grows uniformly. Problems occur as soon as big changes in curvature are observed, which are typical for branching morphogenesis and morphogenesis in general. Figure 6a shows that the minimal distance algorithm fails to map a straight line to the line with a protrusion; no point on C_1 is mapped onto the curve segment between points A and B. Minimal distance mapping strongly depends on the direction of mapping. In many cases reverse minimal distance mapping provides better results (Fig. 6b), because the complexity of the domain structure typically increases rather than decreases during development. Our circle-ellipse example illustrates the limitations of minimal distance mapping (Fig. 5a). The problem can be resolved by reversing the algorithm (Fig. 5b). A slight improvement is observed if we do a transformation beforehand (Fig. 5c).

— *Normal Mapping:* The normal mapping algorithm provides an excellent mapping for the simple test case of a circle and a cylinder (Fig. 5d). Unlike the minimal distance algorithm, the normal mapping algorithm is not very much affected by the curvature of C_2. It is, however, sensitive to the curvature of C_1. If the curvature in locally concave regions of C_1 is comparably higher than the distance between the curves, then crossings of the displacement field vectors can be observed (Fig. 7a). Therefore, the quality of a displacement field computed by normal mapping strongly depends on whether C_1 encloses a concave domain and whether C_2 is far away from these concave regions. This problem is illustrated in Fig. 7a where the two curves look very much alike but are far away from each other and the enclosed domain of C_1 is not convex. This case results in a crossing of the displacement field vectors, which is not desirable. As shown in Fig. 7b this problem is locally solved by doing a reverse mapping. In case of our simple circle-ellipse example we observe that a normal mapping works very well because a circle is a concave domain (Fig. 5d). On the other a hand, a reverse normal mapping in this configuration (Fig. 5e) leads to crossings of the displacement field vectors and large parts of the ellipse are not mapped onto

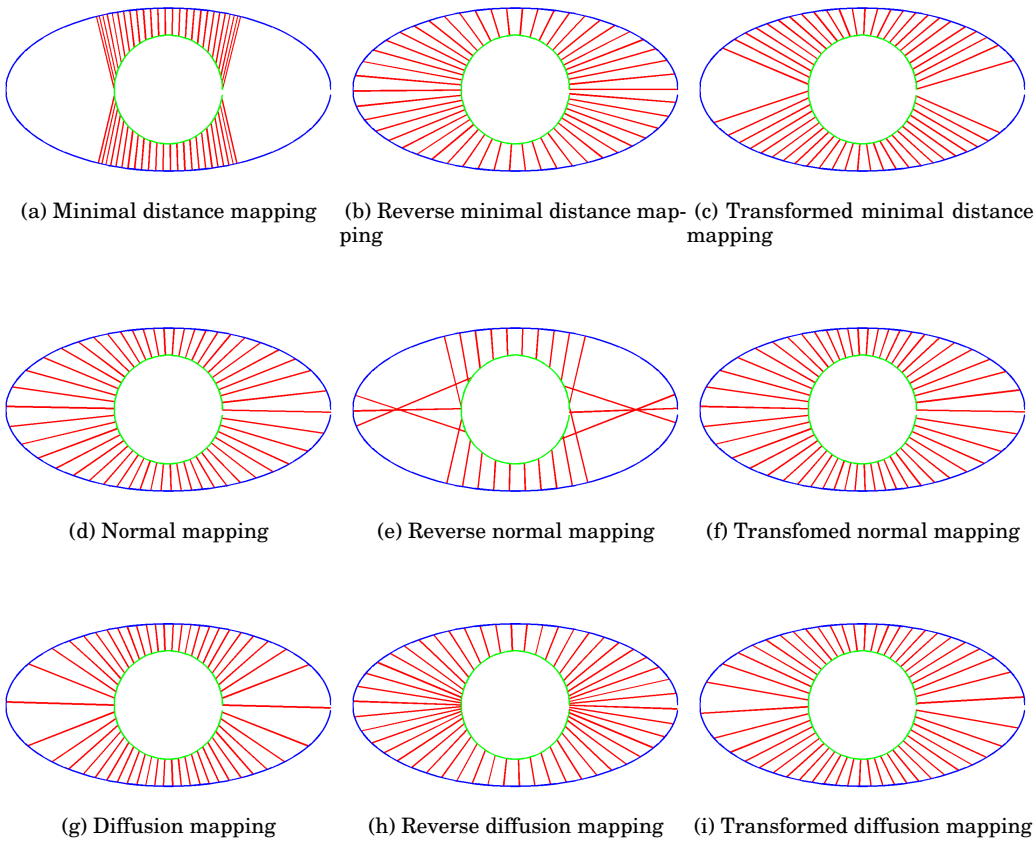

(a) Minimal distance mapping (b) Reverse minimal distance mapping (c) Transformed minimal distance mapping

(d) Normal mapping (e) Reverse normal mapping (f) Transfomed normal mapping

(g) Diffusion mapping (h) Reverse diffusion mapping (i) Transformed diffusion mapping

Fig. 5: **Comparison of Mapping Algorithms with a Simple Test Case.** Displacement fields (red) for the simple mapping problem between C_1, a circle (green) and C_2, an ellipse (blue), as generated by mapping algorithms based on minimal distance, normal vectors, or diffusion, as well as their reverse and transformed versions.

the circle because the normal vectors from these regions fail to reach the circle. This problem can be addressed by a re-scaling of the domains prior to normal mapping (Fig. 5f), such that similar results are obtained as with the original normal mapping.

— *Diffusion Mapping:* Many real world mapping problems can be resolved by only mapping curve segments onto each other, because they often only have one curvature direction, such that we can find a good mappings based on normal or minimal distance mapping, in combination with the appropriate prior transformations. However, if the curvature changes its sign within the subdomain, i.e. if the curve changes between being locally convex or concave (Fig. 8), minimal distance, normal mapping and the reverse mappings all yield bad results in some section of the curve. In Figure 8a, normal mapping gives good results in region B where the curve we are mapping from is locally concave and returns crossings in region A where the curve is locally convex. Minimal distance mapping fails in the opposite situations

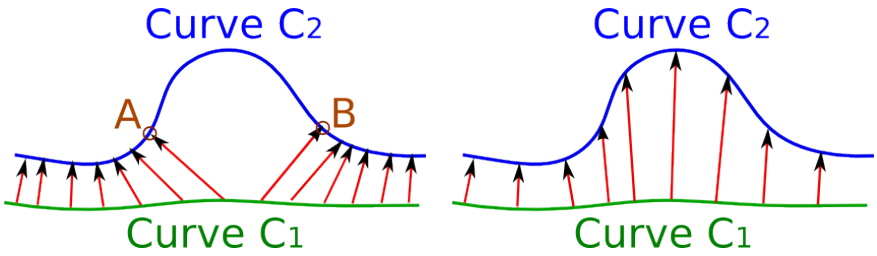

(a) Minimal distance (b) Reverse minimal distance

Fig. 6: **Minimal Distance Mapping.** Every point on the curve C_1 is mapped to the point on the curve C_2 to which it has the minimal distance. If curve C_2 shows big changes in curvature, it is often advisable to use reverse minimal distance mapping. (a) Minimal distance mapping cannot map points onto points in the segment between points A and B. (b) Reverse minimal distance mapping can resolve the issue shown in panel a.

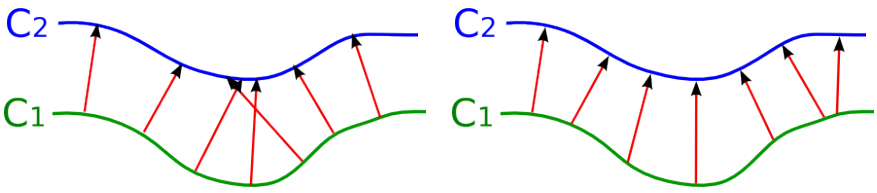

(a) Normal mapping (b) Reverse normal mapping

Fig. 7: **Normal mapping.** (a) If C_1 encloses a non–convex domain and both curves are not very close to each other in these concave regions of C_1, then the displacement field vectors generated by normal mapping cross each other. (b) The problem can be resolved by using reverse normal mapping.

(Fig. 8b) and the reverse mapping will help in neither case due to the symmetry of the problem. Good mapping results can, however, be obtained with diffusion mapping, because the streamlines reach any region of C_2 and will never cross each other. The downside of the diffusion method is that small regions on the generally shorter curve C_1 are mapped onto fairly large regions on C_2 as can be seen in Figure 5g. In this case, the reverse mapping can help (Fig. 5h) as well as a first scaling of C_1 (Fig. 5i).
Diffusion mapping is very safe but does not give overall as good results as normal and minimal distance mapping. Furthermore, it is computationally much more expensive than any of the other mapping algorithms and it is therefore wise to only apply it when normal or minimal distance fail, due to their limitations on curves that have changing curvature sign and lie far apart from each other.

— *Uniform Mapping:* Uniform mapping is the method of choice for open curves with relatively small deformation (Fig. 9a). For closed curves or curve segments between two intersection points this method is advisable only if the curves are relatively short or the changes in curvature are small because the direction of the displacement field is always biased towards the direction of the biggest change in

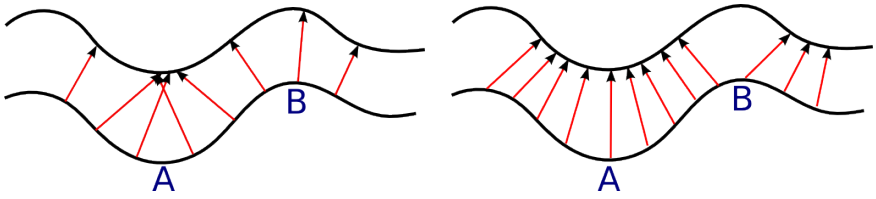

(a) Normal mapping fails (b) Minimal distance fails

Fig. 8: **Normal and Minimal Distance Mapping Fail.** When we try to map curves of changing curvature sign that lie far apart from each other, we run into problems with both minimal distance and normal mapping. We have a symmetric problem that cannot be solved by reversing the algorithm. In (a) we do a normal mapping that leads to crossings in region A that will just lead to crossings in region B when we reverse the algorithm, and in (b) minimal distance gives us bad results in region B since we are ignoring some parts of the curve onto which we are mapping to. This can also not be solved by using reverse minimal distance because the same problem would show up in curve region A.

growth, as can be seen in Figure 9b.

— *Transformed Mapping:* We have applied our basic algorithms to the circle-ellipse example (Fig. 5) and saw that scaling the circle beforehand could lead to an improvement of the displacement field quality. Now we apply the transformation algorithm to our mouse kidney data and compare it qualitatively with the non-transformed algorithm (Fig. 10a). In Figure 10a we see that minimal distance fails in many curve regions. The transformation algorithm first scales and aligns the curve C_1 which results in the dashed curve $C_{1,t}$ (Fig. 10b). Then $C_{1,t}$ is mapped onto C_2 (Fig. 10c). The starting points of the displacement field vectors that lie on $C_{1,t}$, are back transformed onto C_1 such that we get the final displacement field vectors (Fig. 10d). We

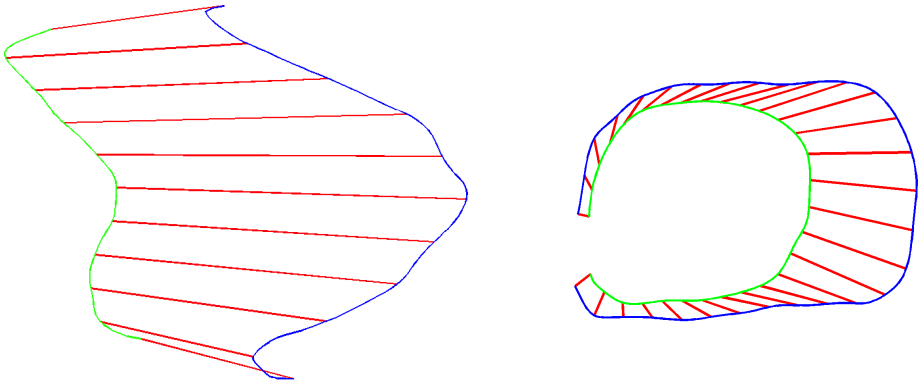

(a) (b)

Fig. 9: **Uniform Mapping** (a) The displacement fields of open curves are determined by interpolating both curves with equidistant points and by mapping the points consecutively onto each other. (b) When the growth of the domain is not uniform, we get a displacement field that is biased towards the direction of maximal growth.

observe that the newly obtained displacement field has a much higher quality than without prior transformation since $C_{1,t}$ and C_2 are on average closer to each other than C_1 to C_2. The downside of this method is that the displacement field vectors are very often distorted, i.e. the angles between the vectors and the C_1 normal vectors are large. When do we want to first scale the curve C_1? The more uniformly the growing domain develops, the better it is to scale C_1 prior to doing the mapping. Usually there are many curve segments $C_{in} \subseteq C_2$ that lie inside the domain bounded by C_1. By scaling, we usually improve the mapping from C_1 to $C_{out} = C_2 \backslash C_{in}$ and worsen the mapping results from C_1 to C_{in}. So it is not advisable to do scaling if C_{in} is large and does not always lie close to C_1. This is often the case if we map C_1 onto a much later developed domain C_2 since the complexity of the curves are increasing and do not only grow uniformly.

In summary, we showed that the different algorithms are suited for different mapping problems. The normal and minimal distance mapping algorithms often produce the nicest displacement fields, but they fail for curves with strong changes in the curvature. The diffusion mapping algorithm rarely fails, but overall gives sub-optimal results.

3.2. Mapping in the Limiting Case of an Infinite Number of Points

In this section we will discuss the mapping algorithms for smooth curves and the consequences in a discrete space. In case of smooth curves, the displacement field algorithm $\mathcal{D}$: $C_1 \rightarrow C_2$, is applied onto all the infinite number of points along the curve C_1 that are mapped onto C_2. We call the mapping well-defined on a subset $\tilde{C}_1 \subseteq C_1$ if $\forall p_1 \in \tilde{C}_1, \exists p_2 = \mathcal{D}(p_1) \in C_2$. Both uniform and diffusion mapping have the properties that $\tilde{C}_1 = C_1$ and the mapping is bijective. These are desirable properties since a deforming domain will neither have boundary points that vanish nor will points contract to a single point. Furthermore, both algorithms have the property that they do not allow crossings of the theoretical displacement field. When we talk about the *crossing* of the displacement field, we mean that each point on C_1 is mapped onto C_2 such that the order in which the points occur along the curve is conserved.

Let us now look at minimal distance and normal mapping and the reverse of both of them. The minimal distance algorithm applied to smooth curves will always return results that are normal to the curve on which they are mapped onto. Therefore, reverse minimal distance and normal mapping as well as minimal distance and reverse normal mapping are intrinsically the same with the only difference that (reverse) minimal distance on a closed and smooth curve only returns a subset of the displacement field that we get by (reverse) normal mapping. Without loss of generality we will only look at the first algorithm pair: normal and reverse minimal distance mapping.

Since the minimal distance algorithm is well-defined on C_1, the reverse minimal distance algorithm maps every point $p_2 \in C_2$ onto a point $p_1 \in C_1$. This means that we find a mapping from a subset of points $\tilde{C}_1$ to all of C_2. Therefore, if a continuous part on $C_1 \backslash \tilde{C}_1$ is mapped onto C_2 using normal mapping, there must be crossings in the displacement field except if all points of $C_1 \backslash \tilde{C}_1$ map to exactly the same point, i. e. they lie on a perfect circle and map to its centre. By this we see that reverse minimal distance discards all the mapping vectors that could lead to crossings. Note that this property no longer holds in regions close to the boundary of two open curves of finite length because minimal distance might map points onto the start and end points of C_2 and these vectors will no longer be normal to the curve.

For our computations it is important to now consider the case where we have a finite number of points that are mapped onto each other.

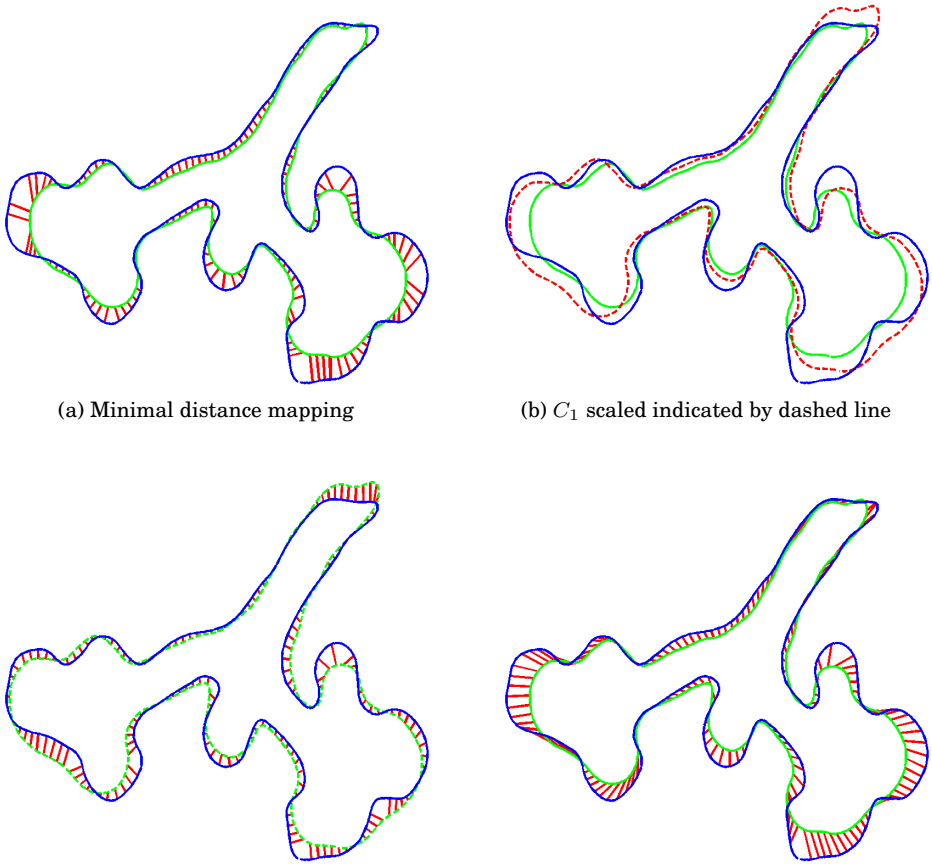

(a) Minimal distance mapping

(b) C_1 scaled indicated by dashed line

(c) Minimal distance mapping from C_t onto C_2

(d) Displacement field starting points are transformed back onto C_1

Fig. 10: **Transformation Prior Mapping.** (a) The displacement field was computed using the basic minimal distance algorithm. (b) By scaling the inner curve C_1 onto the same size as C_2 the two curves got closer to each other. (c) We computed the displacement field from our transformed curve $C_{1,t}$ onto C_2. (d) The starting points of our vectors where then transformed back onto our original curve C_1. We observe that in (d) the number of regions on C_2, onto which no points where mapped to, has decreased and the displacement field quality has therefore increased.

Despite our considerations for the mapping algorithms for smooth curves from above, we mostly observe that normal mapping provides better results than reverse minimal distance for the following three reasons: First of all, if the density of the points that should be mapped is not very high, there will be no crossings for normal mapping and reverse minimal distance would still have its usual problems of missing out some regions on C_1. Secondly, reverse minimal distance yields bad results on the boundary of open curves. Thirdly, in generalisation of the second point, depending on our interpolation method, e.g. when using linear interpolation, our curve will not be smooth. As a result, the displacement field vectors will no longer be perfectly normal

on C_1 and reverse minimal distance will preferably map onto local extrema that are given by the points where C_1 is not smooth. Therefore, if we map closed curves onto each other, it is advisable to first compute the density of the points and do reverse minimal distance mapping if the density exceeds some given density threshold; otherwise we use normal mapping.

3.3. Quantitative Evaluation of the Mapping Algorithms

We now seek to define a measure that quantifies the quality of the displacement field. An important criterium is the uniformity of the mapping: a good mapping should map a small arc length on C_1 also onto a small arc length of C_2, which leads us to the quality measure

$$\mathbf{QM}_1 = \left\langle \left(\frac{L_i}{\alpha l_i} - 1 \right)^2 \right\rangle. \tag{4}$$

Here, l_i is the arc length on C_1 between the points p_i and p_{i+1}, which are mapped onto the points P_i and P_{i+1} on C_2 with arc length L_i between them, as shown in Figure 11. The value α is defined as the the scaling factor such that

$$\alpha = \text{Circumference}(C_2)/\text{Circumference}(C_1) \tag{5}$$

and $< \cdot >$ is the average over all i. The smaller the value $\mathbf{QM}_1$, the better the displacement field. If all segments l_i and L_i on curves C_1 and C_2 respectively have equal length, we have the minimal value, $\mathbf{QM}_1 = 0$. This is naturally the case for uniform mapping.

An alternative measure for the uniformity of the displacement field can be formulated based on the area A_i enclosed by the segments l_i, L_i and mapping vectors (Fig. 11):

$$\mathbf{QM}_2 = \left\langle \left(\frac{A_i}{< A_i >} - 1 \right)^2 \right\rangle \tag{6}$$

where A_i is the area defined by the two arc lengths and the displacement vectors. Finally we can combine the two measures, $\mathbf{QM}_1$ and $\mathbf{QM}_2$, to obtain:

$$\mathbf{QM} = \mathbf{QM}_1 \cdot \mathbf{QM}_2 = \left\langle \left(\frac{L_i}{\alpha l_i} - 1 \right)^2 \right\rangle \cdot \left\langle \left(\frac{A_i}{< A_i >} - 1 \right)^2 \right\rangle \tag{7}$$

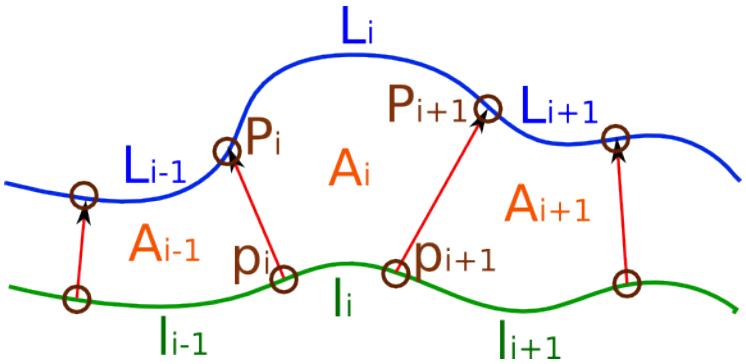

Fig. 11: **Quantifying the Uniformity of the Mapping.** The quality measure (Eq. 4) is based on the segment lengths L_i and l_i between the two mapped points P_i and P_{i+1} and the original points p_i and p_{i+1} respectively. The enclosed surface is defined as A_i.

Table I: Quality measures calculated for the test case of a circle mapped onto an ellipse (Fig. 5). The lowest values for the quality measures are marked in bold.

Mapping	QM_1	QM_2	QM
minimal distance mapping	13.4	22.4	301
reverse minimal distance	**0.128**	**0.134**	**0.017**
transformed minimal distance	1.69	2.71	4.58
normal mapping	0.103	0.398	0.041
reverse normal	56.1	2.45	137
transformed normal	**0.084**	**0.397**	**0.033**
diffusion mapping	0.494	1.17	0.577
reverse diffusion	1.589	**0.088**	0.140
transformed diffusion	**0.224**	0.559	**0.125**

Table I shows the calculated values of QM_1, QM_2 and QM for the simple test case of the circle being mapped onto the ellipse (Fig. 5). The three measures yield the same ranking within the basic algorithms for minimal distance and normal mappings. However, in case of diffusion mapping, QM_1 favours the transformed mapping while QM_2 favours the reverse mapping. The combined measure QM yields the same ranking as QM_1. Visual inspection confirms that all highlighted mappings deliver excellent results (Fig. 5), with QM_1 and QM delivering the most appropriate ranking.

We repeated the analysis with the dataset for *ex vivo* kidney branching morphogenesis [Adivarahan et al. 2013]. We used five datasets and mapped the starting embryonic shape to embryonic datasets that had been acquired after 1h, 2h, 4h, 8h (Table II). As expected, the difference between shapes after 1h of development is so small that the quality measures yield more or less the same results; all our mapping algorithms return good and very similar results. The longer the time difference between the two datasets, the worse the mapping, i.e. the value of our quality measures increases as we map curves that are increasingly distant (Table II). Minimal distance (Fig. 12a) and reverse minimal distance (Fig. 12b) yield rather poor results for big time steps and strong changes in curvature. The same holds for normal and reverse normal mapping where we observe crossings (Fig. 12c and Fig. 12d); as expected there are more crossings for the reverse normal mapping since it maps from a curve with higher changes in curvature to a curve with lower changes in curvature. The poor results of the normal mapping algorithm are in line with our previous observation that normal mapping gives bad results for very big time steps. The algorithm, however, still yields good results for smaller deformations, i.e. until $\Delta \leq 4$h (Table II).

Uniform mapping naturally gives the best results for QM_1 as it lets QM_1 converge to zero by its definition. However, visual inspection reveals that uniform mapping results in slightly distorted displacement fields (Fig. 12g) compared to the reverse diffusion mapping (Fig. 12f). We note that the solution differs substantially from the one obtained with a normal mapping, i.e. the angle between displacement field vectors and the normal vectors are rather large. This is also reflected in QM_2, which identifies the reverse diffusion mapping as the best mapping.

Finally, if we look at QM in Table II, we observe that uniform mapping will again give the best results, since it is almost zero for QM_1. However given the distortions that we get for the uniform mapping, uniform mapping is not necessarily the method

of choice. Based on the QM value, normal mappings yield the second best result for all cases. The QM ranking does not penalize for crossings. In case of crossings, reverse diffusion would be the method of choice. These considerations are taken into account for our final algorithm for the image-based determination of displacement fields.

Table II: Quality measure calculated for the test case of the embryonic kidney branching morphogenesis. The lowest values for the quality measures are marked in bold; the uniform mapping was not considered as it gives the lowest value for QM_1 and QM by definition.

Mapping	$QM_1(\Delta=1h)$	$QM_1(\Delta=2h)$	$QM_1(\Delta=4h)$	$QM_1(\Delta=8h)$
minimal distance	0.027	0.056	0.294	2.03
reverse minimal distance	0.033	0.046	0.144	71.6
normal	**0.010**	**0.031**	**0.089**	**0.281**
reverse normal	0.154	0.108	172	148.9
diffusion	0.019	0.041	0.193	2.03
reverse diffusion	0.077	0.039	0.131	0.559
uniform mapping	0.002	0.011	0.010	0.028
	$QM_2(\Delta=1h)$	$QM_2(\Delta=2h)$	$QM_2(\Delta=4h)$	$QM_2(\Delta=8h)$
minimal distance	0.650	0.809	1.89	5.75
reverse minimal distance	0.587	0.593	1.009	1.748
normal	0.591	0.657	1.04	1.08
reverse normal	0.564	0.531	0.830	1.08
diffusion	0.612	0.833	2.080	6.00
reverse diffusion	**0.506**	**0.510**	**0.795**	**0.811**
uniform mapping	0.599	0.612	0.951	0.999
	$QM(\Delta=1h)$	$QM(\Delta=2h)$	$QM(\Delta=4h)$	$QM(\Delta=8h)$
minimal distance	1.76E-2	4.53E-2	0.556	11.66
reverse minimal distance	1.94E-2	2.73E-2	0.145	125
normal	**0.591E-2**	2.04E-2	**9.25E-2**	**0.304**
reverse normal	8.69E-2	5.73E-2	143	161
diffusion	1.16E-2	3.42E-2	0.401	12.2
reverse diffusion	3.90E-2	**1.99E-2**	0.104	0.454
uniform mapping	0.120E-2	0.673E-2	0.951E-2	0.280

4. DISPLACEMENT FIELDS FOR 3D OBJECTS

In a final step, we extended the basic algorithms to 3D to enable also 3D simulations on growing domains. The only basic algorithm that cannot be used in 3D is uniform mapping. Since computations in 3D can get very expensive, we have used the OPCODE collision detection library [Terdiman 2002] for our normal mapping algorithm. This library efficiently computes ray-mash intersection points by creating a collision tree for the possibly ray intersecting mesh. To determine the computational efficiency of the algorithm, we determined the computational time that is needed to compute an increasing number of displacement field vectors using our normal mapping algorithm for a mesh size of 3'527 and 4'064 mesh-faces of the 3D surface (Fig. 13). As can be seen, the computational time increases linearly with the number of computed displacement field vectors.

Figure 14 shows the mapping of a sphere onto an ellipsoid. We observe the same limitations for minimal distance mapping in 3D (Fig. 14a) that we have seen already in 2D (Fig. 5a). Much as in 2D, the sphere is not mapped to all regions of the ellipsoid. Once again normal mapping (Fig. 14b) and diffusion mapping (Fig. 14c) perform well.

Figure 15 shows the displacement field computed for the embryonic mouse lung epithelium at two developmental stages [Blanc et al. 2012]. Similarly as for the example of a sphere and an ellipsoid, normal mapping and diffusional mapping provide high quality displacement fields, as judged by eye.

5. CONCLUSION

Based on the evaluation of the mapping algorithms we propose a workflow (Algorithm 1 for the 2D case) for the determination of high quality displacement fields from images of subsequent developmental stages. From our overall observations and analysis we learn that it is generally desirable to apply normal mapping as a first attempt. When curves (in 2D) or surfaces (in 3D) intersect, it is advisable to divide the problem into sub-problems according to intersections and then apply the mapping algorithms separately on each segment. If we get a low quality displacement field (e .g. crossings occur), then the normal mapping must be rejected and reverse diffusion mapping can be used. Reverse diffusion mapping is less error–prone when the two curves are far away. In the case of open curves, we can transform the starting and end points of both curves onto each other by translating, rotating and scaling one of the curves, then apply (scaled) normal or reverse diffusion mapping, depending on the crossings as for closed curve segments and finally transform back the curve and the displacement field.

ALGORITHM 1: Algorithm to determine 2D Displacement Fields

Input: Two closed curves C_1 and C_2
Output: Displacement field
if C_1 *and* C_2 *intersect* **then**
    split into subproblems;
else
    consider C_1 and C_2 as one subproblem
end
foreach *subproblem* **do**
    do normal mapping;
    if *crossings* **then**
        do reverse diffusion mapping;
    end
end
return *displacement field;*

In this manuscript, we described and evaluated different algorithms that can be used to compute displacement fields that are required for the simulation of signalling models on growing domains. We have presented four basic algorithms, discussed their properties and presented an algorithm that takes their advantages and disadvantages into account. We must note that our final algorithm does not guarantee a perfect displacement field, nor that the best basic method is used. However, the algorithm works well for many cases and minimises manual curation and modifications of the displacement field, as intended.

Acknowledgements. We thank Edoardo Mazza, Gerald Kress and Simon Tanaka for discussions.

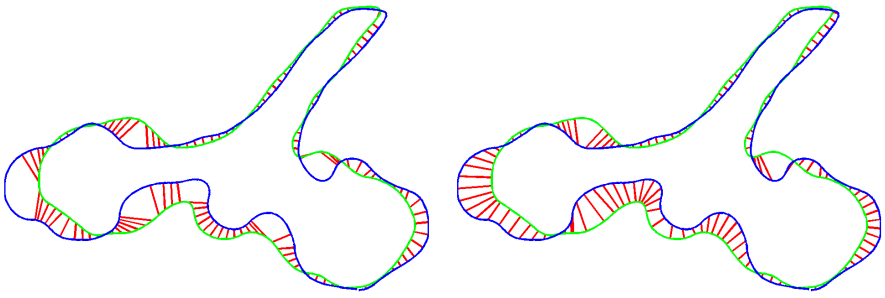

(a) Minimal distance mapping

(b) Reverse minimal distance mapping

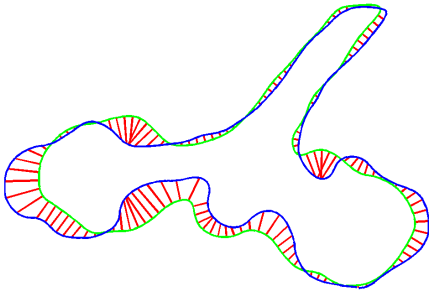

(c) Normal mapping

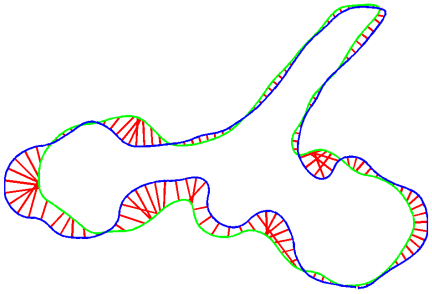

(d) Reverse normal mapping

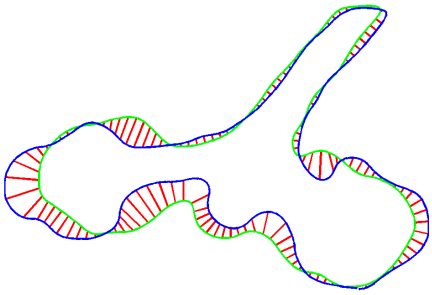

(e) Diffusion mapping

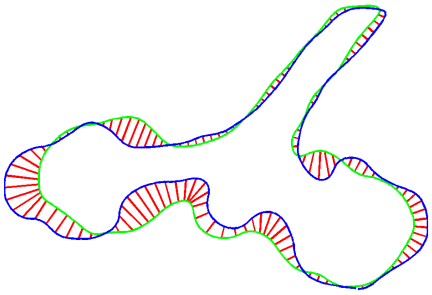

(f) Reverse diffusion mapping

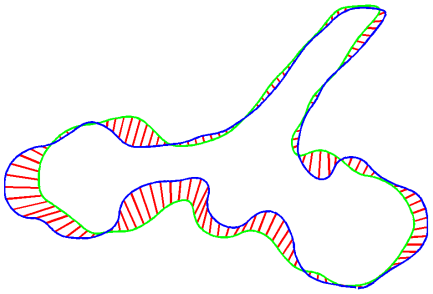

(g) Uniform mapping

Fig. 12: **Mapping of Embryonic Dataset.** Displacement fields generated by different methods for our embryonic dataset of a kidney: C_1 and C_2 represent the shapes of the kidney explant at an initial moment and after 8 hours of development *in vitro*. In all cases we have split our curve into segments before the algorithms where applied.

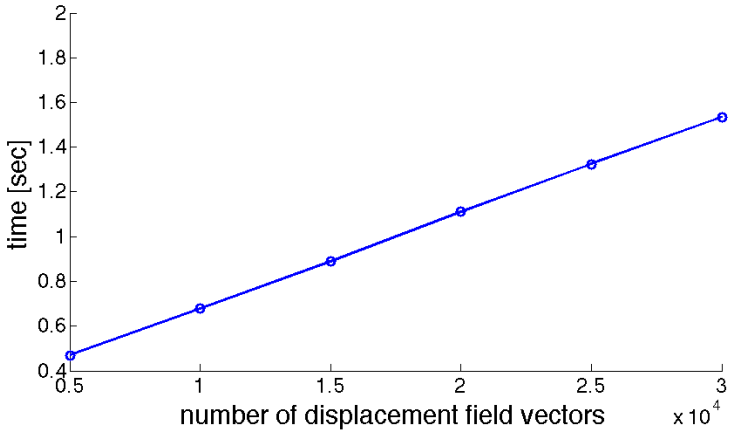

Fig. 13: **Benchmark for 3D Normal Mapping.** Using a mesh size of 3'527 and 4'064 mesh-faces, the computational time increases linearly with the number of computed displacement field vectors.

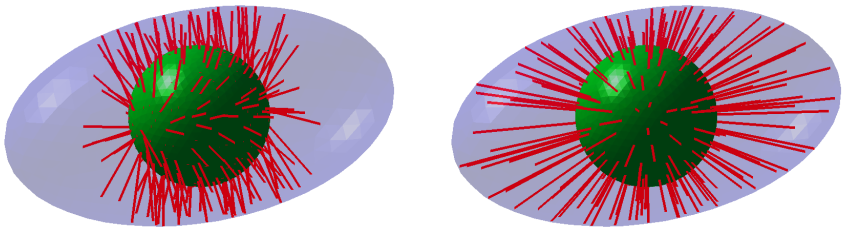

(a) Minimal distance mapping

(b) Normal mapping

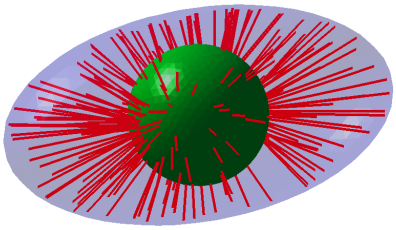

(c) Diffusion mapping

Fig. 14: **3D Minimal Distance and Normal Mapping.** The displacement field from a sphere onto an ellipsoid is computed using (a) minimal distance, (b) normal mapping and (c) diffusion mapping. We observe in (a) that some regions on the ellipsoid cannot be mapped onto and that we get better results in (b) and (c).

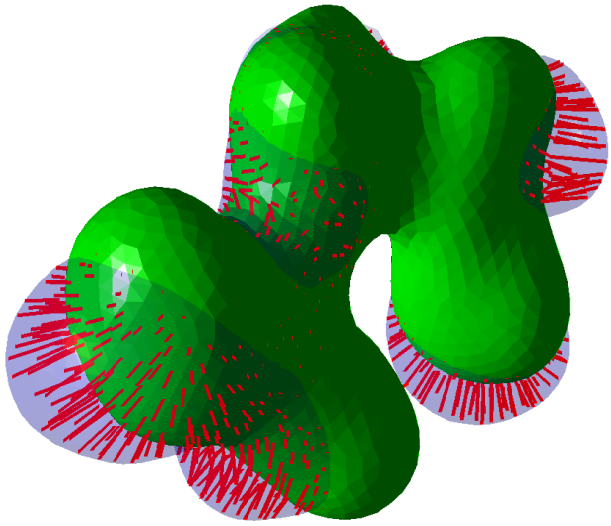

Fig. 15: **Normal Mapping applied to 3D Lung Data.** The displacement field computed by using the normal mapping algorithm.

REFERENCES

Srivathsan Adivarahan, Denis Menshykau, Odyssé Michos, and Dagmar Iber. 2013. Dynamic Image-Based Modelling of Kidney Branching Morphogenesis. In *Computational Methods in Systems Biology*. Springer Berlin Heidelberg, Berlin, Heidelberg, 106–119.

Marc Alexa. 2002. Recent Advances in Mesh Morphing. *Computer graphics forum* 21, 2 (2002), 173–197.

Theodoris Athanasiadis, Ioannis Fudos, Christophoros Nikou, and Vasiliki Stamati. 2010. Feature-based 3D morphing based on geometrically constrained sphere mapping optimization. *Proceedings of the 2010 ACM Symposium on Applied Computing - SAC '10* (2010), 1258.

Amarendra Badugu, Conradin Kraemer, Philipp Germann, Denis Menshykau, and Dagmar Iber. 2012. Digit patterning during limb development as a result of the BMP-receptor interaction. *Scientific reports* 2 (2012), 991.

Y. Bellaïche, F. Bosveld, F. Graner, K. Mikula, M. Remesíková, and M. Smísek. 2011. New robust algorithm for tracking cells in videos of Drosophila morphogenesis based on finding an ideal path in segmented spatio-temporal cellular structures. *Conf Proc IEEE Eng Med Biol Soc* (2011), 6609–12.

Pierre Blanc, Karen Coste, Pierre Pouchin, Jean-Marc Azaïs, Loïc Blanchon, Denis Gallot, and Vincent Sapin. 2012. A role for mesenchyme dynamics in mouse lung branching morphogenesis. *PLoS ONE* 7, 7 (2012), e41643.

Bernd Boehm, Henrik Westerberg, Gaja Lesnicar-Pucko, Sahdia Raja, Michael Rautschka, James Cotterell, Jim Swoger, and James Sharpe. 2010. The role of spatially controlled cell proliferation in limb bud morphogenesis. *PLoS Biol* 8, 7 (0 2010), e1000420. DOI:http://dx.doi.org/10.1371/journal.pbio.1000420

FL Bookstein. 1989. Principal warps: Thin-plate splines and the decomposition of deformations. *IEEE TPAMI* 2 (1989), 567–585.

Geraldine Celliere, Denis Menshykau, and Dagmar Iber. 2012. Simulations demonstrate a simple network to be sufficient to control branch point selection, smooth muscle and vasculature formation during lung branching morphogenesis. *Biology Open* 1, 8 (Aug. 2012), 775–788.

Raphaël Clément, Pierre Blanc, Benjamin Mauroy, Vincent Sapin, and Stéphane Douady. 2012. Shape self-regulation in early lung morphogenesis. *PLoS ONE* 7, 5 (2012), e36925.

John D'Errico. 2012a. distance2curve function. MATLAB Central – File Exchange. (2012). http://www.mathworks.in/matlabcentral/fileexchange/34869-distance2curve

John D'Errico. 2012b. Interparc function. MATLAB Central – File Exchange. (2012). http://www.mathworks.in/matlabcentral/fileexchange/34874-interparc

R. Dillon and H. G. Othmer. 1999. A mathematical model for outgrowth and spatial patterning of the vertebrate limb bud. *J Theor Biol* 197, 3 (4 1999), 295–330. DOI:http://dx.doi.org/10.1006/jtbi.1998.0876

Jason P Gleghorn, Jiyong Kwak, Amira L Pavlovich, and Celeste M Nelson. 2012. Inhibitory morphogens and monopodial branching of the embryonic chicken lung. *Developmental dynamics* 241 (March 2012), 852–862.

Dagmar Iber and Philipp Germann. 2014. How do digits emerge? - mathematical models of limb development. *Birth Defects Res C Embryo Today* 102, 1 (3 2014), 1–12. DOI:http://dx.doi.org/10.1002/bdrc.21057

Dagmar Iber and Denis Menshykau. 2013. The control of branching morphogenesis. *Open Biol* 3, 9 (0 2013), 130088. DOI:http://dx.doi.org/10.1098/rsob.130088

Dagmar Iber, Simon Tanaka, Patrick Fried, Philipp Germann, and Denis Menshykau. 2015. Simulating tissue morphogenesis and signaling. *Methods in molecular biology (Clifton, N.J.)* 1189, Chapter 21 (2015), 323–338.

Dagmar Iber and Rolf Zeller. 2012. Making sense-data-based simulations of vertebrate limb development. *Curr Opin Genet Dev* 22, 6 (Dec. 2012), 570–577.

F. Lazarus and A. Verroust. 1998. Three-dimensional metamorphosis: a survey. *Visual Computer* 14 (1998), 373–389.

Denis Menshykau, Pierre Blanc, Erkan Ünal, Vincent Sapin, and Dagmar Iber. 2014. An Interplay of Geometry and Signaling enables Robust Lung Branching Morphogenesis. *Development* in press (2014).

Denis Menshykau and Dagmar Iber. 2012. Simulating Organogenesis with Comsol: Interacting and Deforming Domains . *Proceedings of COMSOL Conference 2012* (Sept. 2012).

Denis Menshykau and Dagmar Iber. 2013. Kidney branching morphogenesis under the control of a ligand-receptor-based Turing mechanism. *Physical biology* 10, 4 (June 2013), 046003.

Denis Menshykau, Conradin Kraemer, and Dagmar Iber. 2012. Branch Mode Selection during Early Lung Development. *Plos Computational Biology* 8, 2 (Feb. 2012), e1002377.

Luis G Morelli, Koichiro Uriu, Saúl Ares, and Andrew C Oates. 2012. Computational approaches to developmental patterning. *Science* 336, 6078 (April 2012), 187–91.

Andrew C Oates, Nicole Gorfinkiel, Marcos Gonzalez-Gaitan, and Carl-Philipp Heisenberg. 2009. Quantitative approaches in developmental biology. *Nat Rev Genet* 10, 8 (Aug. 2009), 517–530.

Simone Probst, Conradin Kraemer, Philippe Demougin, Rushikesh Sheth, Gail R Martin, Hidetaka Shiratori, Hiroshi Hamada, Dagmar Iber, Rolf Zeller, and Aimée Zuniga. 2011. SHH propagates distal limb bud development by enhancing CYP26B1-mediated retinoic acid clearance via AER-FGF signalling. *Development (Cambridge, England)* 138, 10 (May 2011), 1913–1923.

Ian Sigal, Michael R Hardisty, and Cari M Whyne. 2008. Mesh-morphing algorithms for specimen-specific finite element modeling. *Journal of biomechanics* 41, 7 (2008), 1381–9.

Simon Tanaka and Dagmar Iber. 2013. Inter-dependent tissue growth and Turing patterning in a model for long bone development. *Physical biology* 10, 5 (Oct. 2013), 056009.

Pierre Terdiman. 2002. OPCODE collision detection library. (2002). http://www.codercorner.com/Opcode.htm

Alan M. Turing. 1952. The chemical basis of morphogenesis. *Phil. Trans. Roy. Soc. Lond* B237 (1952), 37–72.

Ortrud Wartlick, Anna Kicheva, and Marcos Gonzalez-Gaitan. 2009. Morphogen gradient formation. *Cold Spring Harbor perspectives in biology* 1, 3 (Sept. 2009), a001255.

O Wartlick, P Mumcu, A Kicheva, T Bittig, C Seum, F Jülicher, and M Gonzalez-Gaitan. 2011. Dynamics of Dpp signaling and proliferation control. *Science* 331, 6021 (March 2011), 1154–1159.

L Wolpert. 1969. Positional information and the spatial pattern of cellular differentiation. *Journal of theoretical biology* 25, 1 (Oct. 1969), 1–47.

APPENDIX A

The details for the transformation algorithm used in section 2.2 are as follows:

— compute the area for both C_1 and C_2, then scale C_1 around its centre of mass to the same area as C_2;
— apply rigid transformation to $C_{1,scaled}$ so that the overlapping area of C_2 and $C_{1,scaled}$ is maximized. Finding an optimal translation and rotation is computationally very expensive and so alternatively we search for the solution using a greedy algorithm and do not go through all possible curve configurations but rather move the curve step by step to the next best configuration until no local improvement can be made (see Algorithm 2). Therefore, we might not find the global optimal solution, but just a locally optimal solution, which, for our purpose, is good enough. We can then use any of the above mentioned algorithms (1) – (4) to compute the mapping from $C_{1,t}$ to C_2. The starting points of these displacement field vectors are then transformed back onto C_1.

ALGORITHM 2: Transformation of Curves

Input: Curve C_1 which is given by N points, curve C_2, step size r, rotation angles θ
Output: Curve $C_{1,transformed}$ which consists of N transformed points
a_1 = area_of_curve(C_1), a_2 = area_of_curve(C_2);
$C_{1,scaled}$ = scale_Curve($C_1, \frac{a_2}{a_1}$);
A_{opt} = curve_intersection_area($C_{1,scaled}$,C_2);
$improvement = TRUE$;
repeat
  $improvement = FALSE$;
  for *each translational direction* ϕ **do**
    for $sign \in \{-1, 1\}$ **do**
      $A_{\theta,old}$ = 0;
      for *each rotation angle* θ **do**
        $C_{1,temp}$ = rotate_curve($C_{1,scaled}$, $sign \cdot \theta$);
        $C_{1,temp}$ = translate_curve($C_{1,temp}$,r,$sign \cdot \phi$);
        $A_{\theta,new}$ = curve_intersection_area($C_{1,temp}$,C_2);
        $\Delta Area = A_{\theta,new} - A_{opt}$;
        if $\Delta Area < 0$ **then**
          $A_{opt} = A_{temp}$;
          $improvement = TRUE$;
        end
        if $Area_{\theta,new} - Area_{\theta,old} < 0$ **then**
          break;
        end
        $Area_{\theta,old} = Area_{\theta,new}$;
      end
    end
  end
until *improvement is FALSE*;